



1 SDUST2020MGCR: a global marine gravity change rate model
2 determined from multi-satellite altimeter data
3 Fengshun Zhu ^{1,2,3}, Jinyun Guo ¹, Huiying Zhang ¹, Lingyong Huang ⁴, Heping Sun ^{2,3},
4 Xin Liu ¹
5 1 College of Geodesy and Geomatics, Shandong University of Science and
6 Technology, Qingdao 266590, China
7 2 State Key Lab of Geodesy and Earth's Dynamics, Innovation Academy for
8 Precision Measurement Science and Technology, Chinese Academy of Sciences,
9 Wuhan 430077, China
10 3 University of Chinese Academy of Sciences, Beijing 100049, China
11 4 State Key Laboratory of Geo-Information Engineering, Xian 710054, China

12
13 Corresponding Author: Jinyun Guo, Email: jinyunguo1@126.com
14

15 Abstract. Investigating global time-varying gravity field mainly depends on
16 GRACE/GRACE-FO gravity data. However, satellite gravity data exhibits low spatial
17 resolution and signal distortion. The satellite altimetry is an important technique for
18 observing global ocean, providing continuous multi-year data that enables the study of
19 high-resolution time-varying marine gravity. This study aims to construct a high-
20 resolution marine gravity change rate (MGCR) model using multi-satellite altimetry
21 data. Initially, multi-satellite altimetry data and ocean temperature-salinity data from
22 1993 to 2019 are utilized to estimate the altimetry sea level change rate (SLCR) and
23 steric SLCR, respectively. Subsequently, the mass-term SLCR is calculated. Finally,
24 based on mass-term SLCR, we construct the global MGCR model on 5'×5' grids
25 (SDUST2020MGCR) applying the spherical harmonic function method and mass
26 load theory. Comparisons and analyses are conducted between SDUST2020MGCR
27 and GRACE2020MGCR resolved from GRACE/GRACE-FO gravity data. The
28 spatial distribution characteristics of SDUST2020MGCR and GRACE2020MGCR
29 are similar in the sea areas where gravity changes significantly, such as the seas near
30 some ocean currents, the western seas of Nicobar Islands, and the southern seas of
31 Greenland. The statistical mean values of SDUST2020MGCR and
32 GRACE2020MGCR in global and local oceans are all positive, indicating that MGCR
33 is rising. Nonetheless, differences in spatial distribution and statistical results exist



34 between SDUST2020MGCR and GRACE2020MGCR, primarily attributable to
35 spatial resolution disparities among altimetry data, ocean temperature-salinity data,
36 and GRACE/GRACE-FO data. Compared with GRACE2020MGCR,
37 SDUST2020MGCR has higher spatial resolution and excludes stripe noise and
38 leakage errors. The high-resolution MGCR model constructed using altimetry data
39 can reflect the long-term marine gravity change in more detail, which is helpful to
40 study Earth mass migration. The SDUST2020MGCR model data is available at
41 <https://zenodo.org/records/10098524> (Zhu et al., 2023b).

42 **1 Introduction**

43 The Earth large-scale mass migration will cause spatiotemporal changes of the
44 Earth gravity field (Li et al., 2021). The ocean accounts for about 71% of the global
45 area, the determination of time-varying marine gravity field is an important research
46 content of the Earth time-varying gravity field. The high-precision and high-
47 resolution spatiotemporal change information of marine gravity field is useful for
48 monitoring related geophysical processes such as the ice melting, ocean dynamic
49 processes and crustal deformation.

50 Investigating the Earth time-varying gravity field mainly relies on repeated
51 observation data of ground gravity and satellite gravity. The large-scale regional
52 gravity field changes can be studied utilizing the multi-year gravity measurement data
53 on the relative gravity surveying network (Liang et al., 2016). The precise gravity
54 field changes in small areas can be investigated using repeated measurement data
55 from absolute gravimeters on gravity stations (Greco et al., 2012). However, the
56 gravimeter observation is costly, and gravimeter marine observation requires a lot of
57 manpower, material and financial resources. The satellite gravity provides the
58 possibility for repeated observations of the Earth large-scale gravity field. At present,
59 the high-low satellite-to-satellite tracking, low-low satellite-to-satellite tracking and
60 satellite gravity gradient measurement technologies have been developed. The
61 successfully launched gravity satellites include CHAMP, GRACE/GRACE-FO and
62 GOCE (Flechtner et al., 2021). Among them, the GRACE/GRACE-FO gravity
63 satellite data is the most widely used. The GRACE/GRACE-FO uses the gravity
64 measurement technology of low-low satellite-to-satellite tracking model, it can obtain
65 time-varying gravity with an accuracy of about 0.1 mGal (Flury and Rummel, 2005)
66 and time-varying equivalent water height with an accuracy of approximately 1 cm



67 (Wahr et al., 2004), but its spatial resolution of one-half wavelength is only 400-500
68 km (Tapley et al., 2004), the resolution is low, and there is large signal distortion and
69 leakage errors.

70 The satellite altimetry technique can quickly and repeatedly obtain high-
71 precision global ocean information, becoming an important means to observe and
72 study the ocean. Products such as mean sea level model, static marine gravity field
73 model, and sea level change dataset can be extracted or derived by using altimetry sea
74 surface height (SSH). The Technical University of Denmark team focuses on model
75 improvement in the Arctic Ocean, utilizing multi-satellite altimetry data to construct
76 the global mean sea level model (Andersen et al., 2021, 2023) and the global marine
77 gravity field model (Andersen and Knudsen, 2020). The Shandong University of
78 Science and Technology (SDUST) team also constructs the global mean sea level
79 model (Yuan et al., 2023) and the marine gravity field model (Zhu et al., 2022) using
80 altimetry data, improving the model accuracy in offshore areas. The European
81 Copernicus Marine Environment Monitoring Service uses altimetry data to produce
82 and release daily and monthly gridded sea level change dataset products (Taburet et
83 al., 2019). The Scripps Institution of Oceanography in the United States also develops
84 the global altimetry marine gravity field model (Sandwell et al., 2021). So far, the
85 altimetry SSH is of centimeter-level accuracy, and the calculated global sea level
86 changes have reached millimeter-level accuracy (Nerem et al., 2010). The global
87 altimetry marine gravity field model has a spatial resolution better than 10 km, and
88 the calculation accuracy is about 1 mGal (Sandwell et al., 2013). However, few
89 studies have applied altimetry means to time-varying marine gravity. This paper aims
90 to utilize multi-satellite altimetry data to construct a global marine gravity change rate
91 (MGCR) model (SDUST2020MGCR).

92 The seawater migration causes changes of the Earth shape and gravity field. In
93 this study, we propose to utilize the sea level change rate (SLCR) to calculate the
94 MGCR. Firstly, multi-satellite altimetry data from 1993 to 2019 are utilized to
95 estimate the long-term altimetry SLCR, and EN4.2.1 ocean temperature and salinity
96 data from 1993 to 2019 are utilized to estimate the long-term steric SLCR. Then, the
97 steric SLCR is subtracted from altimetry SLCR to calculate the mass-term SLCR.
98 Finally, this paper applies the method proposed by Zhu et al. (Zhu et al., 2023a) to
99 estimate long-term MGCR, that is utilizing the mass-term SLCR to construct a global
100 MGCR model based on mass load theory and spherical harmonic function method. In

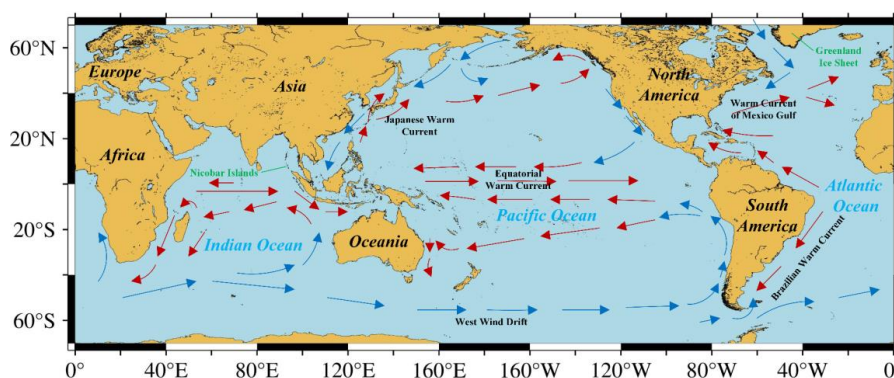


101 Sect. 2, the study area and data sources are introduced. In Sect. 3, the methods of
102 altimetry SLCR estimation, steric SLCR estimation, mass-term SLCR estimation and
103 MGCR estimation are described in detail, respectively. In Sect. 4, the global SLCR
104 and MGCR model are given, and the model comparisons and analyses are performed.
105 In Sect. 5, the conclusion is presented.

106 2 Study area and data

107 2.1 Study area

108 This paper selects the ocean covering 0-360°E and 70°S-70°N as the study area,
109 as shown in Fig. 1. There are various mass migration phenomena on Earth, such as
110 ocean currents that move seawater in a certain direction, the subduction of oceanic
111 plates to continental plates that form island arcs (e.g. Nicobar Islands) and trenches,
112 and the melting ice due to global warming that reduce the mass of Greenland and
113 Antarctic. The mass migration causes changes in the Earth gravity field. Constructing
114 the high-resolution time-varying marine gravity model is helpful for the study of the
115 material migration movement.



116
117 Figure 1. The study area covering 0-360°E and 70°S-70°N. The base map was created using
118 Generic Mapping Tools, then we have roughly marked the Continents, the Oceans and the local
119 sea areas with obvious gravity changes. Red arrows indicate areas where warm currents pass, blue
120 arrows indicate areas where cold currents pass, the Nicobar Islands and Greenland Ice Sheet are
121 also marked.

122 2.2 L2P satellite altimetry data

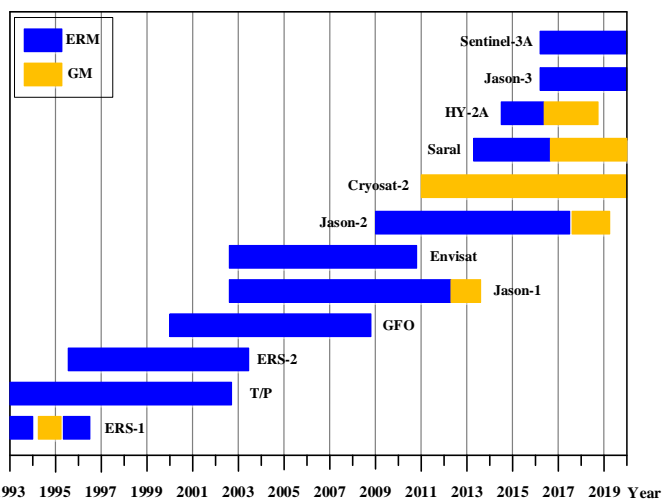
123 The satellite altimetry data includes products at different levels: Level-0 (L0),
124 Level-1 (L1), Level-2 (L2), Level-2 Plus (L2P) and Level-3 (L3). The L0 product is
125 raw telemetered data. The L0 product is corrected for instrumental effects to obtain
126 the L1 product. The L1 product is corrected for geophysical effects to obtain the L2



127 product. The geophysical effects corrections include corrections for dry and wet
128 tropospheric effects, ionospheric effects, ocean state bias, ocean tides, solid tides,
129 polar tides and atmospheric pressure. The L2 product is also called geophysical data
130 records (GDR) product. Based on the L2 product, the correction model is updated and
131 replaced, and the new quality control is carried out, such as data validation, data
132 editing and algorithmic improvement, and finally the L2P product is obtained (CNES,
133 2020). The L3 product is processed river and lake water level time series data.

134 The L2P product is released by the AVISO (Archiving, Validation and
135 Interpretation of Satellite Oceanographic) data center (<https://www.aviso.altimetry.fr/>)
136 of the French Centre National d'Études Spatiales (CNES). The L2P product includes
137 data such as sea level anomaly, mean sea level, environmental parameters, and
138 geophysical correction models. Therefore, the corresponding SSH can be calculated
139 using L2P product as needed. This study utilizes SSH data derived from L2P product
140 to calculate multiple mean sea level models, and construct sea level time series data,
141 and finally the least squares model is applied to estimate high-resolution altimetry
142 SLCR (Yuan et al., 2021).

143 In this study, the L2P product from January 1993 to December 2019 is selected,
144 including two observation mission data of 12 altimetry satellites, as shown in Fig. 2.
145 The ERM (Exact Repeat Mission) data is observed by ERS-1/2, Topex/Poseidon (T/P),
146 Geosat Follow On (GFO), Envisat, Jason-1/2/3, HaiYang-2A (HY-2A), Saral, and
147 Sentinel-3A, and the GM (Geodetic Mission) data is observed by ERS-1, Jason-1/2,
148 HY-2A, Cryosat-2, and Saral.



149



150 Figure 2. The multi-satellite altimetry data utilized in this study. The horizontal axis marks the
151 observation time, and the vertical axis marks the name of the altimetry satellite. Blue represents
152 ERM (Exact Repeat Mission) data, and orange represents GM (Geodetic Mission) data.

153 **2.3 EN4 ocean temperature and salinity data**

154 The ocean temperature and salinity data is important basic data for studying
155 global climate change and ocean change. This data can be used to study seawater
156 volume changes caused by changes in seawater temperature and salinity, and to
157 predict global climate disasters. The Argo (Array for Real-Time Geostrophic
158 Oceanography) project aims to use Argo floats to form a global ocean observation
159 network to measure the depth, temperature, salinity and other data of the ocean in real
160 time (Riser et al., 2016). Now, nearly 4000 Argo floats are in working condition,
161 which provides basic data for constructing global ocean temperature and salinity data
162 products.

163 The various ocean temperature and salinity data products are all affected by
164 irregular floats distribution and model gridding, and their accuracy is basically the
165 same (Hosoda et al., 2008; Roemmich and Gilson, 2009). This study utilizes the
166 EN4.2.1 monthly ocean temperature and salinity product from January 1993 to
167 December 2019 released by the Met Office ([https://argo.ucsd.edu/data/argo-data-
168 products/](https://argo.ucsd.edu/data/argo-data-products/)) to study the seawater volume change and calculate the steric SLCR. The
169 grid size of EN4.2.1 data is $1^{\circ} \times 1^{\circ}$ (Good et al., 2013).

170 **2.4 AVISO monthly sea level anomaly data**

171 The AVISO data center of the CNES also released monthly sea level anomaly
172 data product on $15' \times 15'$ grids. The sea level anomaly is referenced to the mean sea
173 level from 1993 to 2012. This product can resolve sea level changes on a scale of 150-
174 200 km, with an accuracy of centimeter-level in most sea areas around the world
175 (Ducet et al., 2000). The AVISO monthly sea level anomaly data integrates
176 observation data from Jason-1/2/3, T/P, Envisat, ERS-1/2, Geosat and GFO, and has
177 been corrected for geophysical influences, such as dry and wet tropospheric influence,
178 ionospheric delay, tides, and the dynamic atmosphere. This study utilizes AVISO
179 monthly sea level anomaly grid data from January 1993 to December 2019 to estimate
180 AVISO altimetry SLCR.

181 **2.5 ICE-6G glacial isostatic adjustment model**

182 The glacial isostatic adjustment (GIA) is the response of the viscoelastic earth to



183 changes in surface ice and seawater load during the last glacial period. The marine
184 gravity changes resolved from satellite gravity data and satellite altimetry data include
185 not only the impact of contemporary Earth mass migration, but also the impact of
186 solid earth mass redistribution driven by GIA. In the research on various Earth science
187 issues, the GIA effect is usually deducted as a linear term. Argus and Peltier et al.
188 (Argus et al., 2014; Peltier et al., 2015) provided the ICE-6G fully normalized
189 geopotential trend coefficients \dot{C}_{lm}^{GIA} and \dot{S}_{lm}^{GIA} , with the degree and order fully
190 expanded to 256. Based on the ICE-6G fully normalized geopotential trend
191 coefficients, the GIA corrected geopotential coefficients ΔC_{lm}^{GIA} and ΔS_{lm}^{GIA} for each
192 month from January 1993 to December 2019 can also be calculated:

$$193 \quad \begin{cases} \Delta \bar{C}_{lm}^{GIA}(N) = (N/12) \times \dot{C}_{lm}^{GIA} & (N = 1, 2, \dots, 324) \\ \Delta \bar{S}_{lm}^{GIA}(N) = (N/12) \times \dot{S}_{lm}^{GIA} & (N = 1, 2, \dots, 324) \end{cases} \quad (1)$$

194 Where N represents the month, and there are 324 months from January 1993 to
195 December 2019. The GIA corrected geopotential trend coefficients and GIA corrected
196 geopotential coefficients are utilized to correct the altimetry MGCR and
197 GRACE/GRACE-FO monthly gravity data, respectively, which can deduct the marine
198 gravity changes due to the long-term oceanic crust deformation driven by GIA.

199 **2.6 GRACE/GRACE-FO monthly geopotential spherical harmonics data**

200 The main purpose of the GRACE system and the GRACE-FO system is to obtain
201 the long-medium wavelength signals of the Earth gravity field and detect gravity
202 changes (Han et al., 2004). The orbit parameters of GRACE satellite and GRACE-FO
203 satellite are basically the same, with an orbit inclination of 89.5° and an orbit altitude
204 of about 500 km (Wouters et al., 2014). The main instruments carried by the satellites
205 are GPS receivers and ranging systems. The GRACE/GRACE-FO time-varying
206 gravity data mainly consists of Level-1, Level-2 and Level-3. The Level-1 data is
207 satellite orbit data. The Level-2 data is Earth time-varying gravity field model
208 expressed in spherical harmonic coefficient, which has been corrected for the effects
209 of ocean tides, solid tides, atmosphere tides, pole tides, and non-tidal variability in the
210 atmosphere and ocean (UTCSR, 2018). The Level-3 data is grid format data
211 represented by Mascon products.

212 The Center for Space Research at the University of Texas (UTCSR) released
213 GRACE/GRACE-FO Level-2 RL06 monthly geopotential spherical harmonics data,



214 including GSM and GAD data. The CSR_GSM data represents the estimation of
 215 Earth monthly average gravity field, and the degree and order is fully calculated to 60.
 216 The CSR_GAD data represents the impact of non-tidal oceanic and atmospheric
 217 pressure to the ocean bottom pressure. The International Center for Global Earth
 218 Model (ICGEM, <http://icgem.gfz-potsdam.de/home>) provides CSR_GSM data filtered
 219 by DDK2. The DDK2 is non-isotropic filtering method, and CSR_GSM_DDK2
 220 contains less stripe noise.

221 The GRACE/GRACE-FO dataset has 180-months data between April 2002 and
 222 December 2019, and any missing GRACE/GRACE-FO data are not reconstructed in
 223 this study. The degree-1 coefficients supplementation, degree-2 and degree-3
 224 coefficients replacement are performed on CSR_GSM_DDK2 data. In addition, to
 225 match with the satellite altimetry data, the spherical harmonic coefficient of
 226 CSR_GSM_DDK2 and CSR_GAD are summed in a linear manner:

$$227 \quad \begin{cases} \bar{C}_{lm}^{GRACE}(N) = \bar{C}_{lm}^{GSM}(N) + \bar{C}_{lm}^{GAD}(N) \\ \bar{S}_{lm}^{GRACE}(N) = \bar{S}_{lm}^{GSM}(N) + \bar{S}_{lm}^{GAD}(N) \end{cases} \quad (2)$$

228 Utilizing the mean spherical harmonic coefficient of 180-months gravity data as the
 229 reference gravity field, and the GRACE/GRACE-FO geopotential spherical harmonic
 230 coefficient variations $\Delta\bar{C}_{lm}^{GRACE}$ and $\Delta\bar{S}_{lm}^{GRACE}$ are calculated. Then the monthly equivalent
 231 seawater height (ESH) change is obtained (Wahr et al., 1998; Godah, 2019):

$$232 \quad \Delta ESH(N, \lambda, \theta) = \frac{a\rho_E}{3\rho_S} \cdot \sum_{l=0}^{60} \sum_{m=0}^l [(2l+1)/(1+k_l)] \cdot \bar{P}_{lm}(\cos\theta) \cdot [\Delta\bar{C}_{lm}^{GRACE}(N) \cos m\lambda + \Delta\bar{S}_{lm}^{GRACE}(N) \sin m\lambda] \quad (3)$$

233 Where λ and θ are the geocentric longitude and colatitude of the calculation point, a
 234 ($= 6378136.3$ m) is the Earth equatorial radius, ρ_E ($= 5514$ kg/m³) is the Earth
 235 average density, and ρ_S ($= 1028$ kg/m³) is the seawater average density, l and m are
 236 degree and order of spherical harmonic coefficient, \bar{P} is the fully normalized
 237 associated Legendre function, k is the load Love number.

238 In this study, the GIA corrected geopotential coefficient is subtracted from the
 239 GRACE/GRACE-FO geopotential spherical harmonic coefficient variations:

$$240 \quad \begin{cases} \Delta\bar{C}_{lm}(N) = \Delta\bar{C}_{lm}^{GRACE}(N) - \Delta\bar{C}_{lm}^{GIA}(N) \\ \Delta\bar{S}_{lm}(N) = \Delta\bar{S}_{lm}^{GRACE}(N) - \Delta\bar{S}_{lm}^{GIA}(N) \end{cases} \quad (4)$$

241 Then the monthly gravity change is calculated (Godah, 2019):



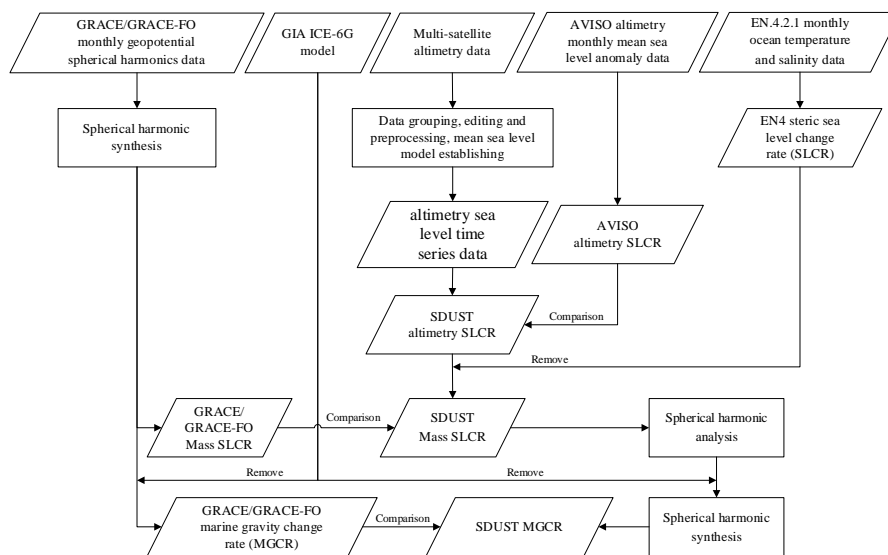
$$\Delta g(N, r, \lambda, \theta) = \frac{GM}{r^2} \sum_{l=0}^{60} \sum_{m=0}^l (l-1) \cdot (a/r)^l \cdot \bar{P}_m(\cos \theta) \cdot [\Delta \bar{C}_{lm}(N) \cos m\lambda + \Delta \bar{S}_{lm}(N) \sin m\lambda] \quad (5)$$

243 Where r is the geocentric radius, GM is the Earth gravitational constant, and other
244 variables are the same as before. This study applies the forward modelling method to
245 correct signal leakage errors on GRACE/GRACE-FO ESH time series data and
246 gravity time series data. Finally, the least squares model is applied to estimate the
247 GRACE/GRACE-FO mass-term SLCR and MGCR, and the grid size is $1^\circ \times 1^\circ$.

248 3 Methodology

249 The submarine plate motion, the melting of glacier and ice sheet, and the change
250 of ocean dynamics all lead to the spatial distribution changes of seawater mass, which
251 in turn causes changes of Earth shape and gravity field. In static marine gravity field
252 studies, the geoid height is obtained by subtracting the mean sea surface topography
253 from the instantaneous altimetry SSH, and then the geoid height or geoid gradient is
254 utilized to construct the gravity field model (Gopalapillai and Mourad, 1979; Hwang
255 et al., 2002). In this study of time-varying marine gravity based on satellite altimetry,
256 the mean sea surface topography is also regarded as invariable, and it is proposed to
257 utilize sea level change to study marine gravity change.

258 The flowchart of this research is shown in Fig. 3. Firstly, following the data
259 grouping, editing and preprocessing of multi-satellite altimetry data, multiple mean
260 sea level models are calculated to construct altimetry sea level time series data, and
261 then the high-resolution SDUST altimetry SLCR is estimated by applying the least
262 squares model and is compared with the AVISO altimetry SLCR. Then the SDUST
263 mass-term SLCR is calculated by subtracting the EN4 steric SLCR from the SDUST
264 altimetry SLCR, and is compared with the GRACE/GRACE-FO mass-term SLCR.
265 Finally, based on the SDUST mass-term SLCR, the spherical harmonic analysis, GIA
266 effect deduction and spherical harmonic synthesis are performed to obtain the SDUST
267 MGCR, and the SDUST MGCR is compared with the GRACE/GRACE-FO MGCR.



268
 269 Figure 3. Flowchart of marine gravity change rate derivation from satellite altimetry data

270 **3.1 Estimation of altimetry SLCR**

271 **3.1.1 Data grouping and editing**

272 The multi-satellite altimetry data from January 1993 to December 2019 are
 273 utilized to construct the high-precision and high-resolution altimetry SLCR model.
 274 The obliquity between the Moon orbit and the Earth equator is called the lunar
 275 declination angle, with a maximum value of 28.5° and a minimum value of 18.5° , and
 276 its change cycle is 18.6 years. This study uses a 19-year moving window and a 1-year
 277 moving step to divide the L2P products into 9 groups (Yuan et al., 2020a), which can
 278 attenuate the ocean effect of a typical tide with 18.6 years. In addition, in order to
 279 improve the modeling accuracy, the low-quality SSH data is excluded according to
 280 the thresholds for altimeter, radiometer and geophysical parameters defined in the L2P
 281 product handbook (CNES, 2020).

282 **3.1.2 Data preprocessing**

283 Each group of SSH data needs to perform the ocean variability correction to
 284 attenuate SSH anomalous variation, SSH seasonal variation and radial orbit error. For
 285 the ERM data, the collinear adjustment method is applied to perform ocean variability
 286 correction (Rapp et al., 1994). The steps of this method are as follows: firstly, the



287 track with the most observation points among all collinear tracks is selected as the
288 reference track; then, the SSH of each point on other period collinear tracks is
289 interpolated to corresponding point on the reference track; finally, the average value
290 of the SSH at each point is calculated to obtain a mean track.

291 The tracks of GM data are not collinear, so the GM data cannot use the collinear
292 adjustment to perform the ocean variability correction. In this study, the ERM data of
293 T/P series satellites (T/P, Jason-1/2/3) is continuous from 1993 to 2019, thus the tracks
294 of T/P series ERM data after collinear adjustment are selected as reference tracks
295 (Yuan et al., 2021). Then, the SSH difference of the T/P series ERM data between the
296 reference track point and the corresponding collinear track point is calculated (Yuan et
297 al., 2020b). Finally, the SSH correction on the GM track is obtained using the space-
298 time objective analysis interpolation (Yuan et al., 2020b; Schaeffer et al., 2012), and
299 the ocean variability correction for GM data of each satellite is performed.

300 The short-wavelength ocean variability signals, radial orbit error residuals and
301 geophysical correction residuals in SSH data still affect the modeling of mean sea
302 level. This study uses the crossover adjustment based on the posteriori compensation
303 theory of error to continue the correction of SSH data. The details of this crossover
304 adjustment method were described by Huang et al and Yuan et al (Huang et al., 2008;
305 Yuan et al., 2020b). The steps of this method are as follows: firstly, the observation
306 equation of altimetry satellite at the crossover point is established, and the conditional
307 adjustment is performed to obtain the SSH correction v at the crossover point; then,
308 for each altimetry track, a mixed polynomial error model $f(t)$ with independent
309 variable of the measurement time t at observation point is established (Yuan et al.,
310 2021):

$$311 \quad f(t) = a_0 + a_1(t - T_0) + \sum_{i=1}^M (b_i \cdot \cos(2\pi i \cdot (t - T_0) / (T_1 - T_0)) + c_i \cdot \sin(2\pi i \cdot (t - T_0) / (T_1 - T_0))) \quad (6)$$

312 Where a_0 , a_1 , b_i and c_i ($i = 1, 2, \dots, M$) are the parameters that need to be determined,
313 the value of M can be determined based on the length of the altimetry track (Huang et



314 al., 2008), the T_0 and T_1 respectively represent the start and end observation time of
315 the altimetry track. The correction v is used as the virtual observation to establish the
316 error equation $v = f(t) + \delta$, δ is observation noise, and the unknown coefficients in $f(t)$
317 are solved by the least squares principle; finally, the solved coefficients and the
318 measurement time t are put in the error model $f(t)$, and the SSH error of each
319 observation point is calculated, and the SSH is corrected.

320 **3.1.3 The mean sea level model establishing**

321 The least squares collocation (LSC) method are excellent at achieving optimal
322 interpolation using the priori information of observations (Jin et al., 2011). In this
323 study, the LSC method is used to establish the mean sea level model on $5' \times 5'$ grids
324 based on the along-track SSH data. The steps of this method are as follows: firstly, the
325 geoid height calculated from the EGM2008 Global Gravity Field model is selected as
326 the reference SSH, and the SSH data subtracts the reference SSH to obtain the
327 residual SSH; then the along-track residual SSH is de-averaged, and gridded applying
328 the LSC method, where the covariance function in the LSC method is described by a
329 second-order Markov process (Jordan, 1972); finally, the average value of the residual
330 SSH is added back to the grid value, and the reference SSH is also recovered, a mean
331 sea level model on $5' \times 5'$ grids is established.

332 **3.1.4 Long-term altimetry SLCR model establishing**

333 This study calculates nine mean sea level models using nine groups of SSH data,
334 which constructs sea level time series data with 1-year interval. Then, we apply the
335 least squares method to estimate the long-term altimetry SLCR. The SDUST global
336 altimetry SLCR model (SDUST_Altimetry_SLCR) on $5' \times 5'$ grids is established, and
337 will be compared with the AVISO global altimetry SLCR model
338 (AVISO_Altimetry_SLCR).

339 **3.2 Estimation of steric SLCR**

340 The changes in ocean temperature and salinity cause the seawater volume
341 changes, which also known as steric SSH changes. The steric SSH change at any
342 location can be calculated using the seawater density change (Llovel et al., 2010):



$$343 \quad \Delta SSH_{Steric}(N, \lambda, \theta) = \frac{1}{\rho_S} \int_{-h}^0 [\rho(N, \lambda, \theta, z, T, S) - \bar{\rho}(\lambda, \theta, z, \bar{T}, \bar{S})] dz \quad (7)$$

344 Where z represents the seawater depth, ρ , T and S are the density, temperature and
 345 salinity of seawater, $\bar{\rho}$, \bar{T} and \bar{S} are the average density, average temperature and
 346 average salinity of seawater from January 1993 to December 2019, h is the distance
 347 from the sea bottom to the sea surface.

348 This study utilizes the EN4.2.1 monthly ocean temperature and salinity data from
 349 January 1993 to December 2019 to calculate the monthly steric SSH changes on a
 350 $1^\circ \times 1^\circ$ grid, and then applies the least squares model to estimate the long-term steric
 351 SLCR. Finally, the EN4 global steric SLCR model (EN4_Steric_SLCR) with $1^\circ \times 1^\circ$
 352 grid size is constructed.

353 3.3 Estimation of mass-term SLCR

354 The altimetry sea level change represents the total sea level change, which
 355 includes seawater volume change and seawater mass change (Yang et al., 2022).
 356 Therefore, the EN4 steric SLCR is subtracted from the SDUST altimetry SLCR:

$$357 \quad SLCR_{Mass} = SLCR_{Altimetry} - SLCR_{Steric} \quad (8)$$

358 Note that the EN4 steric SLCR model, initially defined on $1^\circ \times 1^\circ$ grids, is up-sampled
 359 to $5' \times 5'$ using Kriging interpolation model to facilitate model calculation. Finally, the
 360 SDUST global mass-term SLCR model (SDUST_Mass_SLCR) with $5' \times 5'$ grid size is
 361 constructed, which will be compared with the GRACE/GRACE-FO mass-term SLCR
 362 model.

363 3.4 Estimation of MGCR

364 The Earth have obvious load response to the surface mass change, the load
 365 response includes Earth surface displacement and gravity field change. The Earth
 366 gravity field change by the mass load response can be calculated by applying the
 367 spherical harmonic function method. The spherical harmonic function method can be
 368 divided into two steps: the spherical harmonic analysis and spherical harmonic
 369 synthesis (Sneeuw, 1994; Godah, 2019).

370 Firstly, the global mass-term SLCR is expanded into spherical harmonic
 371 coefficient:



$$\begin{cases} \dot{\bar{C}}_{lm}^{Mass} = \frac{1}{4\pi a} \cdot \frac{3\rho_0}{\rho_{ave}} \cdot \frac{(1+k_f)}{(2l+1)} \cdot \int_0^{2\pi} \int_0^\pi SLCR_{Mass}(\lambda, \theta) \cdot \bar{P}_{lm}(\cos\theta) \cdot \cos m\lambda \cdot \sin\theta d\theta d\lambda \\ \dot{\bar{S}}_{lm}^{Mass} = \frac{1}{4\pi a} \cdot \frac{3\rho_0}{\rho_{ave}} \cdot \frac{(1+k_f)}{(2l+1)} \cdot \int_0^{2\pi} \int_0^\pi SLCR_{Mass}(\lambda, \theta) \cdot \bar{P}_{lm}(\cos\theta) \cdot \sin m\lambda \cdot \sin\theta d\theta d\lambda \end{cases} \quad (9)$$

372 Where $\dot{\bar{C}}_{lm}^{Mass}$ and $\dot{\bar{S}}_{lm}^{Mass}$ are the fully normalized geopotential trend coefficients
 373 corresponding to the mass-term SLCR. The grid size of the SDUST mass-term SLCR
 374 model is 5'×5', so its spherical harmonic coefficient is fully calculated to the 2160
 375 degree. The above process is called spherical harmonic analysis.
 376

377 In order to deduct the GIA effect, this study subtracts the GIA corrected
 378 geopotential trend coefficients $\dot{\bar{C}}_{lm}^{GIA}$ and $\dot{\bar{S}}_{lm}^{GIA}$ from $\dot{\bar{C}}_{lm}^{Mass}$ and $\dot{\bar{S}}_{lm}^{Mass}$:

$$\begin{cases} \dot{\bar{C}}_{lm} = \dot{\bar{C}}_{lm}^{Mass} - \dot{\bar{C}}_{lm}^{GIA} \\ \dot{\bar{S}}_{lm} = \dot{\bar{S}}_{lm}^{Mass} - \dot{\bar{S}}_{lm}^{GIA} \end{cases} \quad (10)$$

380 Then according to the spherical harmonic coefficient and the position information, the
 381 spherical harmonic domain integration is performed:

$$382 \quad MGCR(r, \lambda, \theta) = \frac{GM}{r^2} \sum_{l=0}^{2160} \sum_{m=0}^l (l-1)(a/r)^l \bar{P}_{lm}(\cos\theta) (\dot{\bar{C}}_{lm} \cos m\lambda + \dot{\bar{S}}_{lm} \sin m\lambda) \quad (11)$$

383 The above calculation is also called spherical harmonic synthesis. The SDUST
 384 global MGCR model (SDUST2020MGCR) with a grid size of 5'×5' is obtained using
 385 the spherical harmonic coefficient of degree 2160. The SDUST2020MGCR will be
 386 compared with the GRACE/GRACE-FO MGCR model (GRACE2020MGCR).

387 4 Results and analysis

388 This study calculates the long-term SLCR of the sea area covering 70°S-70°N,
 389 and finally obtains the long-term MGCR. The grid size of models in the study are
 390 inconsistent. Therefore, to enhance the presentation of models for comparison, the
 391 models with grid size smaller than 5'×5' is up-sampled to 5'×5' applying the Kriging
 392 interpolation method. The results are discussed and analyzed below.

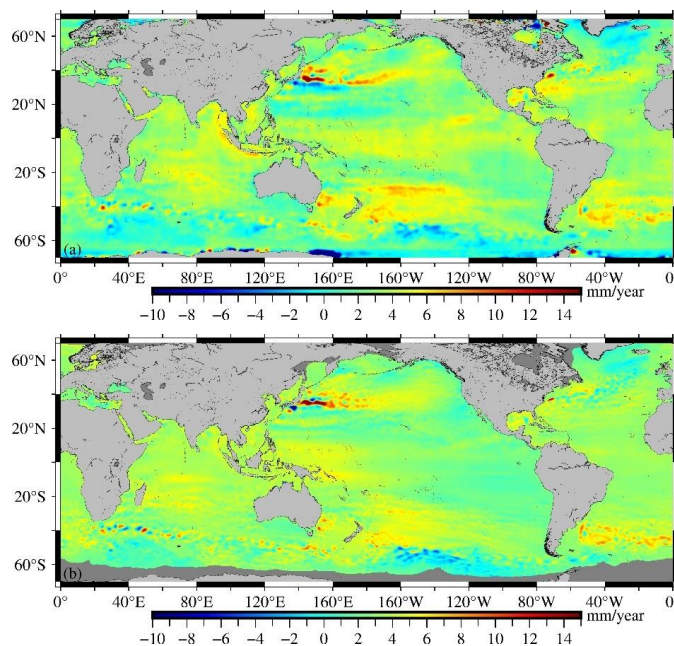
393 4.1 The SLCR model

394 The SDUST_Altimetry_SLCR constructed by using multi-satellite altimetry data
 395 is shown in Fig. 4a. The AVISO_Altimetry_SLCR constructed by using AVISO
 396 monthly sea level anomaly data is shown in Fig. 4b. The Fig. 5 illustrates
 397 EN4_Steric_SLCR constructed using EN4.2.1 ocean temperature and salinity data.
 398 Furthermore, The SDUST_Mass_SLCR obtained by subtracting EN4_Steric_SLCR



399 from SDUST_Altimetry_SLCR is shown in Fig. 6a, and the GRACE_Mass_SLCR
400 resolved from the GRACE/GRACE-FO monthly geopotential spherical harmonic data
401 is presented in Fig. 6b. Upon comparing the results of long-term altimetry SLCR (Fig.
402 4), it is evident that the distribution characteristics of the SDUST_Altimetry_SLCR
403 and the AVISO_Altimetry_SLCR are basically consistent on the global scale. Upon
404 comparing the results of the long-term mass-term SLCR (Fig. 6), there are some
405 differences in the distribution characteristics of SDUST_Mass_SLCR and
406 GRACE_Mass_SLCR on the global scale, however, similarities are identified in local
407 sea areas, such as the eastern seas of Japan, the western seas of the Nicobar Islands,
408 and the southern seas of Greenland.

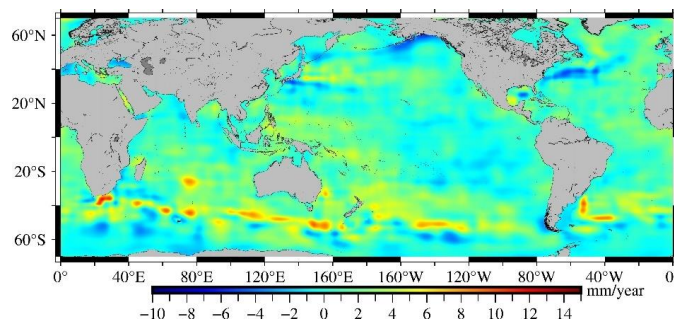
409



410

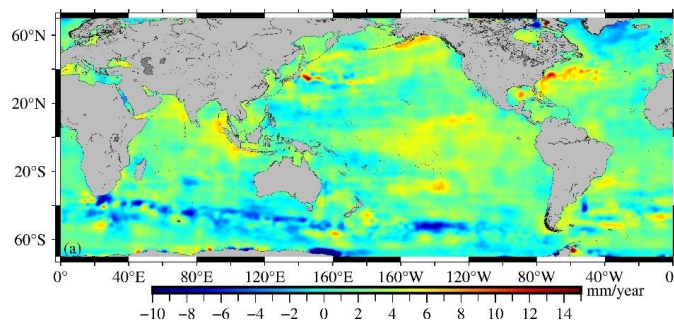
411 Figure 4. The long-term altimetry SLCR. (a) SDUST_Altimetry_SLCR, (b)
412 AVISO_Altimetry_SLCR.

413

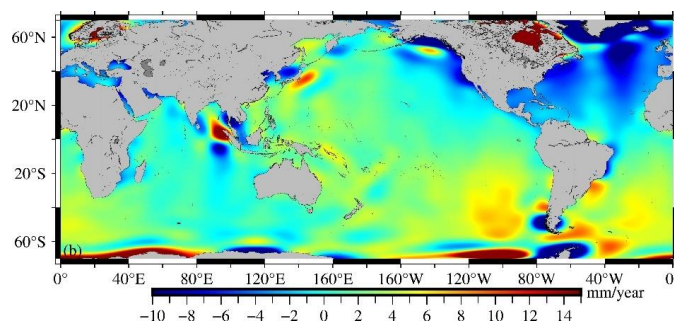




414 Figure 5. The long-term steric SLCR (EN4_Steric_SLCR).



415



416

417 Figure 6. The long-term mass-term SLCR. (a) SDUST_Mass_SLCR, (b) GRACE_Mass_SLCR.

418 The long-term SLCR for the global ocean (60°S~60°N), the Indian Ocean
 419 (20°~105°E, 60°S~30°N), the Pacific Ocean (105°E~80°W, 60°S~60°N) and the
 420 Atlantic Ocean (80°W~20°E, 60°S~60°N) are statistically analyzed, and the results
 421 are shown in Table 1. The statistical results of SDUST_Altimetry_SLCR and
 422 AVISO_Altimetry_SLCR are basically consistent, and the mean value of altimetry
 423 SLCR in the global ocean is all about 3.2 mm/year. There are some differences in the
 424 statistical results of SDUST_Mass_SLCR and GRACE_Mass_SLCR, but the mean
 425 values for both are all positive, signifying an overall upward trend in the mass-term
 426 sea level. In addition, the statistical results show that the standard deviation (STD) of
 427 SDUST_Mass_SLCR is smaller than GRACE_Mass_SLCR. The more detailed
 428 comparative analysis of the results derived from multi-satellite altimetry and
 429 GRACE/GRACE-FO is presented in Sect. 4.2.

430 Table 1. Statistical results of long-term SLCR (mm/year)

SLCR Models	Oceans	Max	Min	Mean	STD
SDUST_Altimetry_SLCR	Global	25.75	-9.66	3.18	1.59
	Indian	13.08	-4.69	3.04	1.65
	Pacific	25.75	-9.66	3.22	1.65
	Atlantic	16.05	-9.07	3.21	1.39
AVISO_Altimetry_SLCR	Global	30.28	-15.55	3.22	1.38



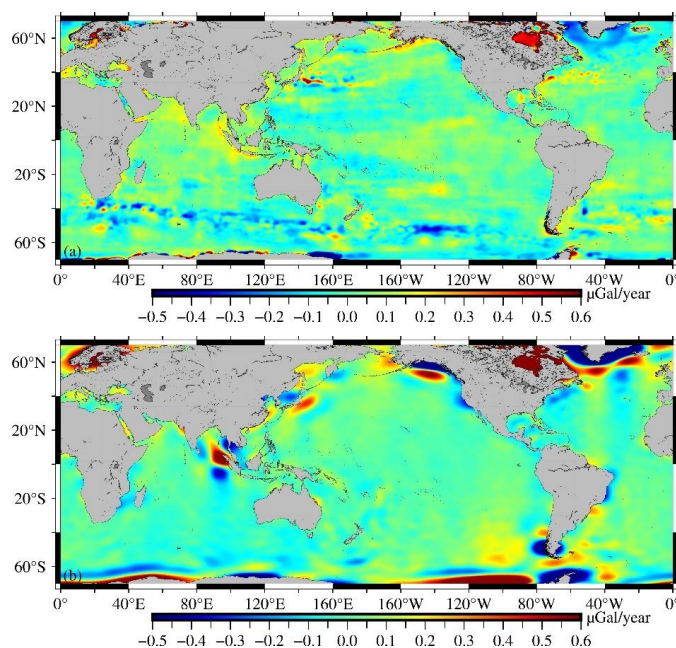
	Indian	14.06	-5.72	3.41	1.25
	Pacific	30.28	-15.55	3.15	1.52
	Atlantic	16.77	-2.55	3.25	1.13
	Global	11.72	-5.94	1.19	1.72
EN4_Steric_SLCR	Indian	11.72	-3.87	1.33	1.97
	Pacific	9.58	-5.94	1.17	1.71
	Atlantic	9.72	-5.01	1.13	1.54
	Global	16.53	-11.52	1.98	1.98
SDUST_Mass_SLCR	Indian	9.57	-11.52	1.70	2.27
	Pacific	16.53	-10.10	2.03	1.97
	Atlantic	14.10	-9.71	2.06	1.75
	Global	44.43	-85.54	1.16	4.46
GRACE_Mass_SLCR	Indian	24.03	-12.42	0.69	2.63
	Pacific	42.90	-85.54	1.75	4.45
	Atlantic	44.43	-53.19	0.27	5.18

431 4.2 The MGCR model

432 The SDUST2020MGCR constructed by applying the spherical harmonic
 433 function method is shown in Fig. 7a, and the GRACE2020MGCR resolved from the
 434 GRACE/GRACE-FO satellite gravity data is shown in Fig. 7b. The
 435 SDUST2020MGCR and GRACE2020MGCR have similar spatial distribution
 436 characteristics in some local sea areas. In the eastern seas of Japan, both
 437 SDUST2020MGCR and GRACE2020MGCR can detect the dipole phenomenon of
 438 marine gravity change, which may be related to the gradually increasing ocean
 439 circulation (Wang and Wu, 2019). The Nicobar Islands in the northeastern Indian
 440 Ocean are located on the collision boundary where the oceanic plate subducts beneath
 441 the continental plate. Both SDUST2020MGCR and GRACE2020MGCR indicate that
 442 the marine gravity in the western seas of the Nicobar Islands is rising, which may be
 443 attributed to the material accumulation caused by plate subduction (Zhu et al., 2023a).
 444 In the southern seas of Greenland, both SDUST2020MGCR and GRACE2020MGCR
 445 exhibit a downward trend, which is related to the mass loss of Greenland due to ice
 446 melting (Groh et al., 2019). In the seas near the West Wind Drift and the Brazilian
 447 Warm Current, both SDUST2020MGCR and GRACE2020MGCR reveal that the
 448 high-frequency signals of marine gravity changes are relatively significant, which
 449 reflects the influence of ocean currents on the marine gravity field. However,
 450 differences exist in the global scale spatial distribution between SDUST2020MGCR
 451 and GRACE2020MGCR. The Fig. 7a shows that GRACE2020MGCR still exhibits
 452 strip noise and may contains leakage errors residuals.



453



454

455 Figure 7. The long-term MGCR. (a) SDUST2020MGCR, (b) GRACE2020MGCR.

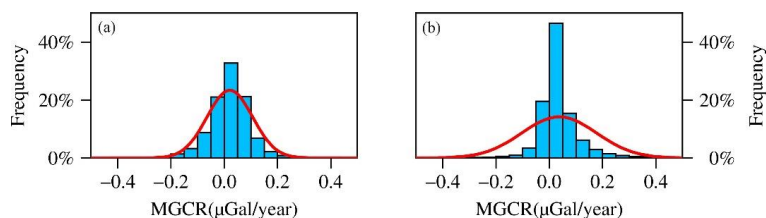
456 The long-term MGCR in the global ocean, the Indian Ocean, the Pacific Ocean
 457 and the Atlantic Ocean are statistically analyzed, and the results are presented in Table
 458 2. The statistical histogram of the long-term MGCR is plotted, as shown in Fig. 8. The
 459 power spectral density of MGCR model is estimated by using the periodogram
 460 method, as illustrated in Fig. 9. The Table 2 shows that the long-term MGCR mean
 461 values for both SDUST2020MGCR and GRACE2020MGCR are positive values in
 462 the global and local oceans. The long-term MGCR mean value in global ocean is
 463 about 0.02 $\mu\text{Gal}/\text{year}$. The statistical results also indicate that the STD of
 464 SDUST2020MGCR is smaller than GRACE2020MGCR. The Fig. 8 shows that the
 465 MGCR value of SDUST2020MGCR and GRACE2020MGCR are mainly between -
 466 0.2 and 0.2 $\mu\text{Gal}/\text{year}$, and SDUST2020MGCR is more consistent with the Gaussian
 467 normal distribution. The Fig. 9 shows that the signal strength of SDUST2020MGCR
 468 is greater than GRACE2020MGCR in the entire frequency domain.

469 Table 1. Statistical results of long-term MGCR ($\mu\text{Gal}/\text{year}$)

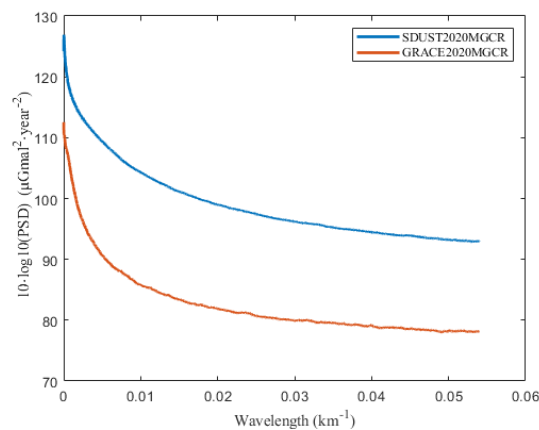
	Oceans	Max	Min	Mean	STD
SDUST2020MGCR	Global	3.28	-1.41	0.02	0.09
	Indian	0.47	-0.44	0.03	0.08
	Pacific	1.37	-0.48	0.02	0.08
	Atlantic	3.28	-1.41	0.03	0.09
GRACE2020MGCR	Global	1.00	-3.60	0.03	0.14



Indian	1.00	-0.51	0.01	0.10
Pacific	0.95	-3.60	0.03	0.14
Atlantic	0.94	-1.52	0.06	0.15



470
 471 Figure 8. The statistical histogram of the long-term MGCR. (a) SDUST2020MGCR, (b)
 472 GRACE2020MGCR.



473
 474 Figure 9. The power spectral density of MGCR model.

475 There are some differences in spatial distribution and statistical results between
 476 SDUST2020MGCR and GRACE2020MGCR, which are mainly related to the
 477 following factors: (1) The spatial resolution of the GRACE/GRACE-FO monthly
 478 gravity data is low, its signal contains north-south strip noise and leakage errors, and
 479 both error correction processing and error residuals make real geophysical signals
 480 distorted and weak. (2) The satellite altimetry data exhibits relatively high spatial
 481 resolution, but its time-varying marine gravity may be affected by SSH measurement
 482 errors. (3) The EN4.2.1 ocean temperature and salinity data suffer accuracy problems
 483 that arise from irregular spatial data distribution and model gridding. Consequently,
 484 the spatial distribution and statistics of SDUST2020MGCR and GRACE2020MGCR
 485 are challenging to mutually validate.

486 5 Data availability

487 The global marine gravity change rate model (SDUST2020MGCR) can be



488 downloaded on the website of <https://zenodo.org/records/10098524> (Zhu et al.,
489 2023b). The dataset contains geospatial information (latitude, longitude) and marine
490 gravity change rates.

491 **6 Conclusions**

492 This study utilized multi-satellite altimetry data and ocean temperature-salinity
493 data from 1993 to 2019 to estimate the global mass-term SLCR. Based on the
494 spherical harmonic function method and mass load theory, we constructed the global
495 MGCR model (SDUST2020MGCR) on 5'×5' grids. This model provides the more
496 detailed information of changes in the marine gravity field.

497 The SDUST2020MGCR and the GRACE/GRACE-FO global MGCR model
498 (GRACE2020MGCR) were compared. In local sea areas where marine gravity
499 changes significantly, such as the eastern seas of Japan, the western seas of the
500 Nicobar Islands, and the southern seas of Greenland, the SDUST2020MGCR and
501 GRACE2020MGCR have certain similarities in spatial distribution. However, there
502 are some differences in the global spatial distribution between SDUST2020MGCR
503 and GRACE2020MGCR, which is mainly related to the mismatch in spatial
504 resolution among satellite altimetry data, satellite gravity data, and ocean temperature-
505 salinity data. Compared with the low-resolution GRACE2020MGCR, the
506 SDUST2020MGCR not only has a higher spatial resolution, but also excludes the
507 strip noise and leakage errors, so it can more realistically reflect the long-term
508 changes in the marine gravity field.

509 The marine gravity changes are the comprehensive result of mass migration in
510 various layers of the Earth, such as the oceanosphere and lithosphere. Utilizing the
511 high-resolution MGCR model derived from multi-satellite altimetry data, and
512 integrating it with other Earth dataset, will be helpful to study the Earth material
513 migration.

514 **Author contributions.**

515 FZ and JG designed the research and developed the algorithm. HZ downloaded
516 altimeter data and other data. FZ carried out the experimental results and wrote the
517 manuscript. LH, HS and XL gave related comments for this work.

518 **Competing interests.**

519 The contact author has declared that none of the authors has any competing interests.



520 **Disclaimer.**

521 Publisher's note: Copernicus Publications maintains neutrality regarding jurisdictional
522 claims in published maps and institutional affiliations.

523 **Acknowledgements.**

524 We appreciate AVISO for providing altimeter data and monthly sea level anomaly
525 data, the UK Met Office for contributing EN4.2.1 data, and the ICGEM for releasing
526 GRACE/GRACE-FO monthly geopotential spherical harmonics data. Special thanks
527 to Professors Peltier and Argus for sharing ICE-6G GIA model. Finally, we would
528 also like to thank the Generic Mapping Tools and its contributors.

529 **Financial support.**

530 This study receives partial support from the National Natural Science Foundation of
531 China (grant Nos. 42192535, 42274006 and 42242015), the Autonomous and
532 Controllable Project for Surveying and Mapping of China (grant No. 816-517), and
533 the Shandong University of Science and Technology Research Fund (grants No.
534 2014TDJH101).

535 **References**

- 536 Andersen, O. B. and Knudsen, P.: The DTU17 Global Marine Gravity Field: First
537 Validation Results, in: Fiducial Reference Measurements for Altimetry, Cham, 83–87,
538 https://doi.org/10.1007/1345_2019_65, 2020.
- 539 Andersen, O. B., Abulaitjiang, A., Zhang, S., and Rose, S. K.: A new high resolution
540 Mean Sea Surface (DTU21MSS) for improved sea level monitoring, Copernicus
541 Meetings, <https://doi.org/10.5194/egusphere-egu21-16084>, 2021.
- 542 Andersen, O. B., Rose, S. K., Abulaitjiang, A., Zhang, S., and Fleury, S.: The DTU21
543 Global Mean Sea Surface and First Evaluation, ESSD – Ocean/Physical oceanography,
544 <https://doi.org/10.5194/essd-2023-160>, 2023.
- 545 Argus, D. F., Peltier, W. R., Drummond, R., and Moore, A. W.: The Antarctica
546 component of postglacial rebound model ICE-6G_C (VM5a) based on GPS
547 positioning, exposure age dating of ice thicknesses, and relative sea level histories,
548 *Geophysical Journal International*, 198, 537–563, <https://doi.org/10.1093/gji/ggu140>,
549 2014.
- 550 CNES: Along-track Level-2+ (L2P) SLA Product Handbook, SALP-MU-P-EA-
551 23150-CLS, Issue 2.0,
552 [https://www.aviso.altimetry.fr/fileadmin/documents/data/tools/hdbk_L2P_all_mission
553 s_except_S3.pdf](https://www.aviso.altimetry.fr/fileadmin/documents/data/tools/hdbk_L2P_all_mission_s_except_S3.pdf) (last access: 6 November 2023), 2020.
- 554 Ducet, N., Le Traon, P. Y., and Reverdin, G.: Global high-resolution mapping of ocean
555 circulation from TOPEX/Poseidon and ERS-1 and -2, *J. Geophys. Res.*, 105, 19477–
556 19498, <https://doi.org/10.1029/2000JC900063>, 2000.



- 557 Flechtner, F., Reigber, C., Rummel, R., and Balmino, G.: Satellite Gravimetry: A
558 Review of Its Realization, *Surv Geophys*, 42, 1029–1074,
559 <https://doi.org/10.1007/s10712-021-09658-0>, 2021.
- 560 Flury, J. and Rummel, R. (Eds.): Future satellite gravimetry and earth dynamics,
561 Springer, Dordrecht, 163 pp., 2005.
- 562 Godah, W.: IGiK–TVGMF: A MATLAB package for computing and analysing
563 temporal variations of gravity/mass functionals from GRACE satellite based global
564 geopotential models, *Computers & Geosciences*, 123, 47–58,
565 <https://doi.org/10.1016/j.cageo.2018.11.008>, 2019.
- 566 Good, S. A., Martin, M. J., and Rayner, N. A.: EN4: Quality controlled ocean
567 temperature and salinity profiles and monthly objective analyses with uncertainty
568 estimates: THE EN4 DATA SET, *J. Geophys. Res. Oceans*, 118, 6704–6716,
569 <https://doi.org/10.1002/2013JC009067>, 2013.
- 570 Gopalapillai, G. S. and Mourad, A. G.: Detailed gravity anomalies from Geos 3
571 satellite altimetry data, *J. Geophys. Res.*, 84, 6213–6218,
572 <https://doi.org/10.1029/JB084iB11p06213>, 1979.
- 573 Greco, F., Currenti, G., D’Agostino, G., Germak, A., Napoli, R., Pistorio, A., and Del
574 Negro, C.: Combining relative and absolute gravity measurements to enhance volcano
575 monitoring, *Bull Volcanol*, 74, 1745–1756, [https://doi.org/10.1007/s00445-012-0630-](https://doi.org/10.1007/s00445-012-0630-0)
576 0, 2012.
- 577 Groh, A., Horwath, M., Horvath, A., Meister, R., Sørensen, L. S., Barletta, V. R.,
578 Forsberg, R., Wouters, B., Ditmar, P., Ran, J., Klees, R., Su, X., Shang, K., Guo, J.,
579 Shum, C. K., Schrama, E., and Shepherd, A.: Evaluating GRACE Mass Change Time
580 Series for the Antarctic and Greenland Ice Sheet—Methods and Results, *Geosciences*,
581 9, 415, <https://doi.org/10.3390/geosciences9100415>, 2019.
- 582 Han, S.-C., Jekeli, C., and Shum, C. K.: Time-variable aliasing effects of ocean tides,
583 atmosphere, and continental water mass on monthly mean GRACE gravity field:
584 TEMPORAL ALIASING ON GRACE GRAVITY FIELD, *J. Geophys. Res.*, 109,
585 <https://doi.org/10.1029/2003JB002501>, 2004.
- 586 Hosoda, S., Ohira, T., and Nakamura, T.: A monthly mean dataset of global oceanic
587 temperature and salinity derived from Argo float observations, *JAMSTEC-R*, 8, 47–
588 59, <https://doi.org/10.5918/jamstecr.8.47>, 2008.
- 589 Huang, M., Zhai, G., Ouyang, Y., Lu, X., Liu, C., and Wang, R.: Integrated Data
590 Processing for Multi-Satellite Missions and Recovery of Marine Gravity Field, *Terr.*
591 *Atmos. Ocean. Sci.*, 19, 103, [https://doi.org/10.3319/TAO.2008.19.1-2.103\(SA\)](https://doi.org/10.3319/TAO.2008.19.1-2.103(SA)), 2008.
- 592 Hwang, C., Hsu, H.-Y., and Jang, R.-J.: Global mean sea surface and marine gravity
593 anomaly from multi-satellite altimetry: applications of deflection-geoid and inverse
594 Vening Meinesz formulae, *Journal of Geodesy*, 76, 407–418,
595 <https://doi.org/10.1007/s00190-002-0265-6>, 2002.
- 596 Jin, T., Li, J., Jiang, W., and Wang, Z.: The new generation of global mean sea surface
597 height model based on multi-altimetric data, *Acta Geodaetica et Cartographica Sinica*,
598 40, 723–729, 2011.



- 599 Jordan, S. K.: Self-consistent statistical models for the gravity anomaly, vertical
600 deflections, and undulation of the geoid, *J. Geophys. Res.*, 77, 3660–3670,
601 <https://doi.org/10.1029/JB077i020p03660>, 1972.
- 602 Li, Q., Bao, L., and Shum, C. K.: Altimeter-derived marine gravity variations reveal
603 the magma mass motions within the subaqueous Nishinoshima volcano, Izu–Bonin
604 Arc, Japan, *J Geod*, 95, 46, <https://doi.org/10.1007/s00190-021-01488-7>, 2021.
- 605 Liang, W., Zhang, G., Zhu, Y., Xu, Y., Guo, S., Zhao, Y., Liu, F., and Zhao, L.: Gravity
606 variations before the Menyuan Ms 6.4 earthquake, *Geodesy and Geodynamics*, 7,
607 223–229, <https://doi.org/10.1016/j.geog.2016.04.013>, 2016.
- 608 Llovel, W., Guinehut, S., and Cazenave, A.: Regional and interannual variability in
609 sea level over 2002–2009 based on satellite altimetry, Argo float data and GRACE
610 ocean mass, *Ocean Dynamics*, 60, 1193–1204, <https://doi.org/10.1007/s10236-010-0324-0>, 2010.
- 612 Nerem, R. S., Chambers, D. P., Choe, C., and Mitchum, G. T.: Estimating Mean Sea
613 Level Change from the TOPEX and Jason Altimeter Missions, *Marine Geodesy*, 33,
614 435–446, <https://doi.org/10.1080/01490419.2010.491031>, 2010.
- 615 Peltier, W. R., Argus, D. F., and Drummond, R.: Space geodesy constrains ice age
616 terminal deglaciation: The global ICE-6G_C (VM5a) model, *JGR Solid Earth*, 120,
617 450–487, <https://doi.org/10.1002/2014JB011176>, 2015.
- 618 Rapp, R. H., Yi, Y., and Wang, Y. M.: Mean sea surface and geoid gradient
619 comparisons with TOPEX altimeter data, *J. Geophys. Res.*, 99, 24657–24667,
620 <https://doi.org/10.1029/94JC00918>, 1994.
- 621 Riser, S. C., Freeland, H. J., Roemmich, D., Wijffels, S., Troisi, A., Belbéoch, M.,
622 Gilbert, D., Xu, J., Pouliquen, S., Thresher, A., Le Traon, P.-Y., Maze, G., Klein, B.,
623 Ravichandran, M., Grant, F., Poulain, P.-M., Suga, T., Lim, B., Sterl, A., Sutton, P.,
624 Mork, K.-A., Vélez-Belchí, P. J., Ansorge, I., King, B., Turton, J., Baringer, M., and
625 Jayne, S. R.: Fifteen years of ocean observations with the global Argo array, *Nature*
626 *Clim Change*, 6, 145–153, <https://doi.org/10.1038/nclimate2872>, 2016.
- 627 Roemmich, D. and Gilson, J.: The 2004–2008 mean and annual cycle of temperature,
628 salinity, and steric height in the global ocean from the Argo Program, *Progress in*
629 *Oceanography*, 82, 81–100, <https://doi.org/10.1016/j.pocean.2009.03.004>, 2009.
- 630 Sandwell, D., Garcia, E., Soofi, K., Wessel, P., Chandler, M., and Smith, W. H. F.:
631 Toward 1-mGal accuracy in global marine gravity from CryoSat-2, Envisat, and
632 Jason-1, *The Leading Edge*, 32, 892–899, <https://doi.org/10.1190/tle32080892.1>, 2013.
- 633 Sandwell, D. T., Harper, H., Tozer, B., and Smith, W. H. F.: Gravity field recovery
634 from geodetic altimeter missions, *Advances in Space Research*, 68, 1059–1072,
635 <https://doi.org/10.1016/j.asr.2019.09.011>, 2021.
- 636 Schaeffer, P., Faugère, Y., Legeais, J. F., Ollivier, A., Guinle, T., and Picot, N.: The
637 CNES_CLS11 Global Mean Sea Surface Computed from 16 Years of Satellite
638 Altimeter Data, *Marine Geodesy*, 35, 3–19,
639 <https://doi.org/10.1080/01490419.2012.718231>, 2012.
- 640 Sneeuw, N.: Global spherical harmonic analysis by least-squares and numerical



- 641 quadrature methods in historical perspective, *Geophysical Journal International*, 118,
642 707–716, <https://doi.org/10.1111/j.1365-246X.1994.tb03995.x>, 1994.
- 643 Taburet, G., Sanchez-Roman, A., Ballarotta, M., Pujol, M.-I., Legeais, J.-F., Fournier,
644 F., Faugere, Y., and Dibarboure, G.: DUACS DT2018: 25 years of reprocessed sea
645 level altimetry products, *Ocean Sci.*, 15, 1207–1224, <https://doi.org/10.5194/os-15-1207-2019>, 2019.
- 647 Tapley, B. D., Bettadpur, S., Ries, J. C., Thompson, P. F., and Watkins, M. M.:
648 GRACE Measurements of Mass Variability in the Earth System, *Science*, 305, 503–
649 505, <https://doi.org/10.1126/science.1099192>, 2004.
- 650 UTCSR: Gravity Recovery and Climate Experiment UTCSR Level-2 processing
651 standards document, Issue5.0, [http://icgem.gfz-](http://icgem.gfz-potsdam.de/GRACE_CSR_L2_Processing_Standards_Document_for_RL06.pdf)
652 [potsdam.de/GRACE_CSR_L2_Processing_Standards_Document_for_RL06.pdf](http://icgem.gfz-potsdam.de/GRACE_CSR_L2_Processing_Standards_Document_for_RL06.pdf) (last
653 access: 6 November 2023), 2018.
- 654 Wahr, J., Molenaar, M., and Bryan, F.: Time variability of the Earth’s gravity field:
655 Hydrological and oceanic effects and their possible detection using GRACE, *J.*
656 *Geophys. Res.*, 103, 30205–30229, <https://doi.org/10.1029/98JB02844>, 1998.
- 657 Wahr, J., Swenson, S., Zlotnicki, V., and Velicogna, I.: Time-variable gravity from
658 GRACE: First results: TIME-VARIABLE GRAVITY FROM GRACE, *Geophys. Res.*
659 *Lett.*, 31, n/a-n/a, <https://doi.org/10.1029/2004GL019779>, 2004.
- 660 Wang, Y.-L. and Wu, C.-R.: Enhanced Warming and Intensification of the Kuroshio
661 Extension, 1999–2013, *Remote Sensing*, 11, 101, <https://doi.org/10.3390/rs11010101>,
662 2019.
- 663 Wouters, B., Bonin, J. A., Chambers, D. P., Riva, R. E. M., Sasgen, I., and Wahr, J.:
664 GRACE, time-varying gravity, Earth system dynamics and climate change, *Rep. Prog.*
665 *Phys.*, 77, 116801, <https://doi.org/10.1088/0034-4885/77/11/116801>, 2014.
- 666 Yang, Y., Feng, W., Zhong, M., Mu, D., and Yao, Y.: Basin-Scale Sea Level Budget
667 from Satellite Altimetry, Satellite Gravimetry, and Argo Data over 2005 to 2019,
668 *Remote Sensing*, 14, 4637, <https://doi.org/10.3390/rs14184637>, 2022.
- 669 Yuan, J., Guo, J., Liu, X., Zhu, C., Niu, Y., Li, Z., Ji, B., and Ouyang, Y.: Mean sea
670 surface model over China seas and its adjacent ocean established with the 19-year
671 moving average method from multi-satellite altimeter data, *Continental Shelf*
672 *Research*, 192, 104009, <https://doi.org/10.1016/j.csr.2019.104009>, 2020a.
- 673 Yuan, J., Guo, J., Niu, Y., Zhu, C., and Li, Z.: Mean Sea Surface Model over the Sea
674 of Japan Determined from Multi-Satellite Altimeter Data and Tide Gauge Records,
675 *Remote Sensing*, 12, 4168, <https://doi.org/10.3390/rs12244168>, 2020b.
- 676 Yuan, J., Guo, J., Zhu, C., Hwang, C., Yu, D., Sun, M., and Mu, D.: High-resolution
677 sea level change around China seas revealed through multi-satellite altimeter data,
678 *International Journal of Applied Earth Observation and Geoinformation*, 102, 102433,
679 <https://doi.org/10.1016/j.jag.2021.102433>, 2021.
- 680 Yuan, J., Guo, J., Zhu, C., Li, Z., Liu, X., and Gao, J.: SDUST2020 MSS: a global 1’
681 × 1’ mean sea surface model determined from multi-satellite altimetry data, *Earth Syst.*
682 *Sci. Data*, 15, 155–169, <https://doi.org/10.5194/essd-15-155-2023>, 2023.



683 Zhu, C., Guo, J., Yuan, J., Li, Z., Liu, X., and Gao, J.: SDUST2021GRA: global
684 marine gravity anomaly model recovered from Ka-band and Ku-band satellite
685 altimeter data, *Earth Syst. Sci. Data*, 14, 4589–4606, [https://doi.org/10.5194/essd-14-](https://doi.org/10.5194/essd-14-4589-2022)
686 4589-2022, 2022.

687 Zhu, F., Liu, X., Li, Z., Yuan, J., Guo, J., and Sun, H.: High spatial resolution marine
688 gravity trend determined from multisatellite altimeter data over Bay of Bengal,
689 *Geophysical Journal International*, 235, 2257–2267,
690 <https://doi.org/10.1093/gji/ggad368>, 2023a.

691 Zhu, F., Guo, J., Zhang, H., Huang, L., Sun, H., and Liu, X.: SDUST2020MGCR: a
692 global marine gravity change rate model determined from multi-satellite altimeter
693 data, Zenodo [data set], <https://doi.org/10.5281/zenodo.10098524>, 2023b.

694

695